



Limits on the Spin–Orbit Angle and Atmospheric Escape for the 22 Myr Old Planet AU Mic b*

Teruyuki Hirano¹, Vigneshwaran Krishnamurthy¹, Eric Gaidos², Heather Flewelling³, Andrew W. Mann⁴, Norio Narita^{5,6,7,8,9}, Peter Plavchan¹⁰, Takayuki Kotani^{7,8,11}, Motohide Tamura^{7,8,12}, Hiroki Harakawa¹³, Klaus Hodapp¹⁴, Masato Ishizuka¹², Shane Jacobson¹⁴, Mihoko Konishi¹⁵, Tomoyuki Kudo¹³, Takashi Kurokawa^{7,16}, Masayuki Kuzuhara^{7,8}, Jun Nishikawa^{7,8,11}, Masashi Omiya^{7,8}, Takuma Serizawa¹⁶, Akitoshi Ueda⁸, and Sébastien Vievard^{7,13}

¹ Department of Earth and Planetary Sciences, Tokyo Institute of Technology, 2-12-1 Ookayama, Meguro-ku, Tokyo 152-8551, Japan; hirano@geo.titech.ac.jp

² Department of Earth Sciences, University of Hawai‘i at Mānoa, Honolulu, HI 96822, USA

³ Institute for Astronomy, University of Hawaii at Mānoa, Honolulu, HI 96822, USA

⁴ Department of Physics & Astronomy, University of North Carolina at Chapel Hill, Chapel Hill, NC 27559, USA

⁵ Komaba Institute for Science, The University of Tokyo, 3-8-1 Komaba, Meguro, Tokyo 153-8902, Japan

⁶ JST, PRESTO, 3-8-1 Komaba, Meguro, Tokyo 153-8902, Japan

⁷ Astrobiology Center, NINS, 2-21-1 Osawa, Mitaka, Tokyo 181-8588, Japan

⁸ National Astronomical Observatory of Japan, NINS, 2-21-1 Osawa, Mitaka, Tokyo 181-8588, Japan

⁹ Instituto de Astrofísica de Canarias (IAC), E-38205 La Laguna, Tenerife, Spain

¹⁰ Department of Physics and Astronomy, George Mason University, 4400 University Drive, MSN 3F3, Fairfax, VA 22030, USA

¹¹ Department of Astronomy, School of Science, The Graduate University for Advanced Studies (SOKENDAI), 2-21-1 Osawa, Mitaka, Tokyo, Japan

¹² Department of Astronomy, Graduate School of Science, The University of Tokyo, 7-3-1 Hongo, Bunkyo-ku, Tokyo 113-0033, Japan

¹³ Subaru Telescope, 650 N. Aohoku Place, Hilo, HI 96720, USA

¹⁴ University of Hawaii, Institute for Astronomy, 640 N. Aohoku Place, Hilo, HI 96720, USA

¹⁵ Faculty of Science and Technology, Oita University, 700 Dannoharu, Oita 870-1192, Japan

¹⁶ Institute of Engineering, Tokyo University of Agriculture and Technology, 2-24-16, Nakacho, Koganei, Tokyo, 184-8588, Japan

Received 2020 May 27; revised 2020 July 10; accepted 2020 July 17; published 2020 August 7

Abstract

We obtained spectra of the pre-main-sequence star AU Microscopii during a transit of its Neptune-sized planet to investigate its orbit and atmosphere. We used the high-dispersion near-infrared spectrograph InfraRed Doppler (IRD) on the Subaru telescope to detect the Doppler “shadow” from the planet and constrain the projected stellar obliquity. Modeling of the observed planetary Doppler shadow suggests a spin–orbit alignment of the system ($\lambda = -4.7_{-6.4}^{+6.8}$ deg), but additional observations are needed to confirm this finding. We use both the IRD data and spectra obtained with NIRSPEC on Keck II to search for absorption in the 1083 nm line of metastable triplet He I by the planet’s atmosphere and place an upper limit for the equivalent width of 3.7 mÅ at 99% confidence. With this limit and a Parker wind model we constrain the escape rate from the atmosphere to $<0.15\text{--}0.45 M_{\oplus} \text{Gyr}^{-1}$, comparable to the rates predicted by an X-ray and ultraviolet energy-limited escape calculation and hydrodynamic models, but refinement of the planet mass is needed for rigorous tests.

Unified Astronomy Thesaurus concepts: [High resolution spectroscopy \(2096\)](#); [Exoplanet evolution \(491\)](#); [Radial velocity \(1332\)](#)

1. Introduction

Detection and characterization of exoplanets in stellar clusters, young moving groups, and even younger star-forming regions can be used to test models of planet formation and evolution, including cooling and contraction (e.g., Vazan et al. 2018), loss of light-element atmospheres (e.g., Ginzburg et al. 2018; Owen 2019), and orbital evolution (e.g., Spalding & Batygin 2016). Such planets have been discovered using the radial velocity (RV) technique (e.g., Sato et al. 2007; Quinn et al. 2012), and more recently with the photometric (transit) method by the K2 mission (e.g., David et al. 2016, 2019; Mann et al. 2016a, 2016b, 2018). The TESS mission is now surveying the entire sky for transiting planets, finding systems with host stars that span a greater range of ages (including moving group members), and they are closer and brighter and

hence more amenable to characterization (e.g., Newton et al. 2019; Mann et al. 2020).

Using TESS photometry, Plavchan et al. (2020) discovered a Neptune-sized planet ($R_p = 4.3R_{\oplus}$) on a 8.5 day transiting orbit around the M star AU Microscopii (AU Mic), a member of the ≈ 20 Myr old β Pictoris moving group (Mamajek & Bell 2014) and the second nearest known pre-main-sequence star. The star possesses a well-studied debris disk (e.g., Grady et al. 2020). Given the proximity (9.7 pc) and brightness ($V = 8.6$) of its host star, AU Mic b is an unparalleled opportunity to study the properties of an infant planet, particularly by spectroscopic observations during transits.

We observed AU Mic during a single transit of “b” to constrain the planet’s orbit and detect any (escaping) atmosphere. The stellar obliquity with respect to the planetary orbit can be measured using the Rossiter–McLaughlin (RM) effect (e.g., Winn et al. 2005). This obliquity reflects the dynamical history of a planetary system; a measurement for a very young system offers more leverage to test different scenarios, including planet migration and planet–planet scattering (e.g., Fabrycky & Tremaine 2007; Nagasawa & Ida 2011; Kley & Nelson 2012). A planet’s extended or escaping atmosphere can

* Based on data collected at Subaru Telescope, which is operated by the National Astronomical Observatory of Japan, and the W. M. Keck Observatory, which is supported by the W. M. Keck Foundation and operated by the California Institute of Technology, the University of California and the National Aeronautics and Space Administration.

be detected via transit-associated absorption. The infrared (1083 nm) lines of metastable “triplet” He I are accessible from the ground. The escape of H/He-rich envelopes could be responsible for a “Neptune desert” (Lundkvist et al. 2016) and a “radius valley” (e.g., Fulton et al. 2017) found in the exoplanet radius–period distribution. The proliferation of RV-capable echelle spectrographs operating in the near-infrared has made simultaneous observations of RM and the He I line possible, as we demonstrate here.

2. Observations and Data Reduction

2.1. Subaru/IRD

On UT 2019 June 17, a transit of AU Mic b was observed with the InfraRed Doppler (IRD) spectrograph ($\lambda/\Delta\lambda \approx 70,000$, $\lambda = 930\text{--}1740$ nm; Tamura et al. 2012; Kotani et al. 2018) on the Subaru telescope. Since AU Mic was too low in elevation when the transit ingress started, we missed the first 15 minutes of the transit. We continuously observed the target with individual integrations of 60 seconds for about 3.8 hours covering the rest of the transit. We suspended the observation of AU Mic about 40 minutes after the egress, and obtained spectra of the A0 star HIP 98926 at a similar airmass for telluric correction. After taking several spectra of HIP 98926, we resumed the observation of AU Mic until the end of the night. As explained in Kuzuhara et al. (2018), raw IRD data were reduced using IRAF software as well as our custom codes. The extracted 1D spectra had a per-pixel signal-to-noise ratio (S/N) of 100–120 at 1000 nm.

2.2. Keck II/NIRSPEC

Y-band (947–1121 nm) spectra of AU Mic were obtained with NIRSPEC (McLean et al. 1998) on the Keck II telescope on Maunakea. The high-resolution echelle mode with a $0''.288$ (3 pixel) \times $12''$ slit delivers $\lambda/\Delta\lambda \approx 37,500$. The star was observed from UT 2019 June 17 MJD = 58,651.419967, after ingress, at an airmass of 2.95, until MJD = 58,651.602753, well after egress and when the star was at an airmass of 1.65. AB nodding was performed for sky subtraction, with the A and B beams separated along the slit by $6''.3$ or 44 pixels. The integration time per beam was 59 seconds and readout used MCDS (four-read double-sampling). A total of 194 integrations were obtained but only 94 A–B beam pairs were usable. The A0 star HD 152849 was observed for telluric correction immediately before the start of AU Mic observations. Flat fields and darks were obtained with the same integration time (1.47 seconds) and a master flat was produced by median combination. Per-pixel S/N in the vicinity of the He I line was 450–2200 per integration, with a median of 1700. A–B beam image pairs were differenced, flattened, and the orders extracted using custom Python scripts. The He I line appeared in two adjacent orders (70 and 71) but 71 suffered from lower S/N and artifacts near the array edge and only 70 was used.

2.3. UH 2.2 m/SNIFS

AU Mic was simultaneously observed with the Super-Nova Integral Field Spectrograph (SNIFS) on the UH 2.2 m telescope on Maunakea. SNIFS uses a lenslet array to re-image a target onto gratings in separate blue (320–520 nm) and red (510–870 nm) channels with $\lambda/\Delta\lambda \approx 900$ (Lantz et al. 2004). Per-pixel, per-integration S/N was about 650, 210,

and 145 in the H I Balmer α , β , and γ lines, respectively. Spectra were extracted and wavelength calibrated using flat-fields and arcs taken at the same pointing. 71 spectra of AU Mic were obtained over four hours between MJD = 58,651.4367 and 58,651.6064. Spectra of telluric calibration stars (HR 4468, GD 153, BD+332642, HR 7596, HR 7950) were obtained before and after AU Mic. Spectra were extracted by the automatic SNIFS pipeline and equivalent widths of H α , β , and γ lines were measured in the intervals 655.4–657.5, 485.4–486.9, and 433.2–434.8 nm, respectively, with the continuum obtained from adjacent ~ 1 nm wide intervals.

3. Analyses and Results

3.1. RV Analysis and Modeling of the RM Effect

To estimate the stellar obliquity, we first analyzed the effective RVs during the transit. Putting the 1D IRD spectra into the RV pipeline, we measured relative RVs for AU Mic (Appendix Appendix). The RV data exhibited a bump around the expected egress, but the lack of ingress and baseline RVs prevented us from evaluating the obliquity. To constrain the projected stellar obliquity λ , we attempted to fit the observed RVs. After some attempts to do this with different subsets of data and different assumptions on the baseline and priors, however, we found that we were unable to obtain a reliable estimate for λ from our RV data set, mostly due to the lack of out-of-transit RV data and unknown behavior of activity-induced RV variations (Appendix). Hence, we decided to determine λ using an alternative technique, Doppler-shadow measurements.

3.2. Doppler-shadow Analysis

Partial occultation of the rotating stellar disk by a transit is manifested as a distortion in the stellar line (e.g., Hirano et al. 2010). Since the cross-correlation function (CCF) of an observed spectra against a template reflects the instantaneous line profile, the time sequence of the CCF residual from the mean out-of-transit CCF exhibits a time-varying anomaly representing a planet’s Doppler “shadow” and this technique has been used to measure the obliquity of host stars (e.g., Collier Cameron et al. 2010; Johnson et al. 2017).

We performed the Doppler-shadow analysis for the IRD spectra, following Hirano et al. (2020a). In computing the CCF, we used a template spectrum representing an early M star, generated from observed IRD spectra of GJ 436 (Hirano et al. 2020b). For each frame, the spectrum for each echelle order was cross-correlated against the template, and we normalized the resulting CCF so that the pseudo-continuum of the CCF wings became unity. In Hirano et al. (2020a), we summed the CCFs for individual orders before the normalization so that the combined CCF conserved the S/N information for each order. However, we found that a similar analysis for AU Mic’s spectra resulted in a low-frequency CCF modulation in time, which differed in each order (left two panels of Figure 1). This sort of modulation was previously seen in our analysis (Gaidos et al. 2020; Hirano et al. 2020a), and mostly originates from a gradual variation of the blaze function, time-varying telluric lines, and/or the detector’s persistence. These modulations could be removed, for example by fitting a low-order polynomial to the out-of-transit CCF data and interpolating the variation during the transit. For AU Mic’s IRD data,

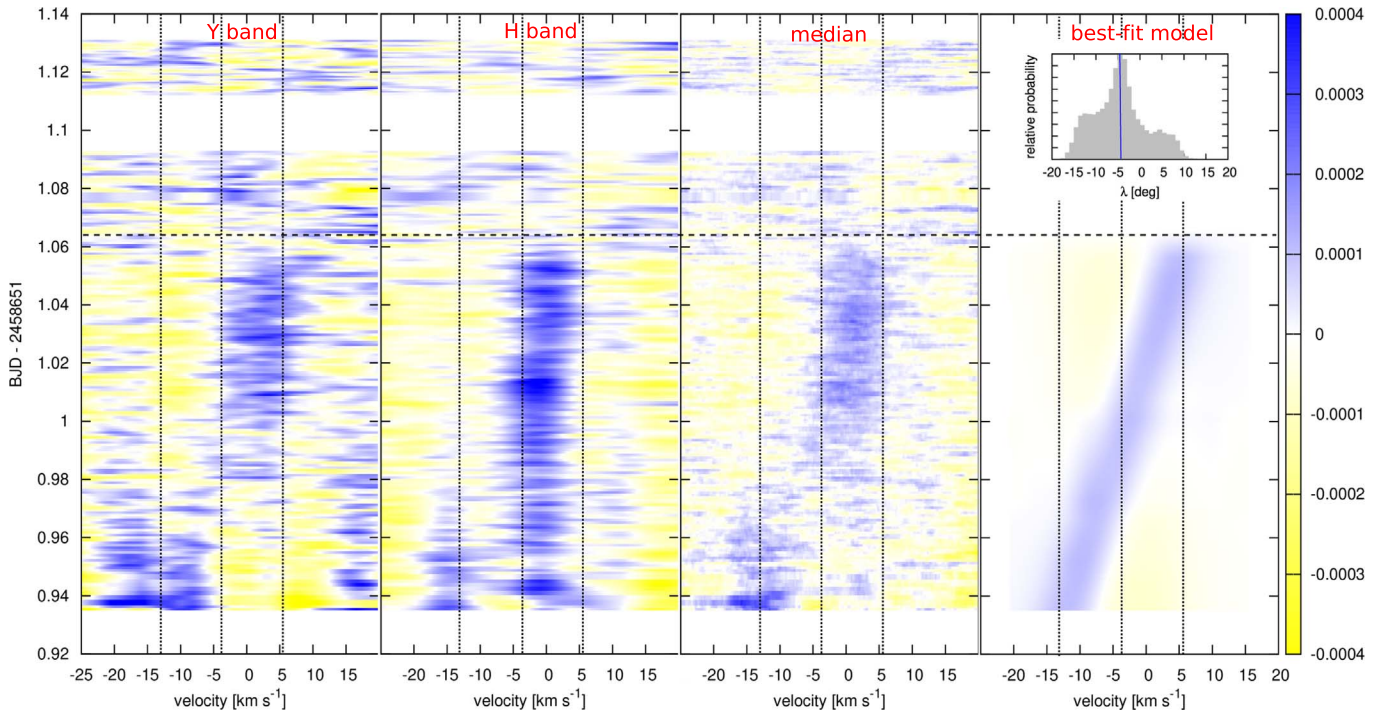


Figure 1. Residual cross-correlation function (CCF) maps for InfraRed Doppler spectra. The left two panels illustrate the combined CCFs for the Y-band orders (leftmost) and H-band orders (second left). The H-band spectra are more vulnerable to telluric lines, and affected by the detector’s persistence. For reference, we obtained $\lambda = 7.7^{+4.7}_{-4.6}$ deg and $\lambda = 85.1^{+1.4}_{-1.1}$ deg for the Y-band and H-band maps, respectively, but those estimates are severely affected by the systematic CCF noise. The third panel from the left displays the median-combined residual CCF map using all available orders. The rightmost panel is the best-fit model for the median-combined CCF map, and its inset displays the posterior distribution of λ for the Markov chain Monte Carlo fit. For each panel, the three vertical dotted lines indicate the CCF line center (middle), representing the barycentric radial velocity of AU Mic, and $\pm v \sin i$ from the center. The horizontal dashed line represents the transit end time.

however, we lacked the ingress and baseline spectra before the transit, and we were unable to remove those modulations by such processing.

To remove the order-dependent CCF modulation, we first subtracted the mean out-of-transit CCF from the individual CCF for each order. We then combined the residual CCFs for all orders by median to obtain the final residual CCFs. This way of combining CCFs does not properly reflect the S/N information for individual orders, but we found through our experience that this processing can suppress the low-frequency modulation in the resulting residual CCF.

The third panel from the left in Figure 1 depicts this extracted residual CCF as a function of time, after Doppler-shifting each frame by the barycentric motion of the Earth. The planet shadow, manifested as a CCF bump, appears to move from the blueshifted part of the profile to the redshifted side and disappears at the expected transit end time (BJD–2,458,651 \approx 1.06). In order to model this residual CCFs, we computed a number of theoretical CCFs following Hirano et al. (2020a). We created mock IRD spectra during the transit for different planet positions on the stellar disk, and put those spectra into the CCF calculations. Based on these theoretical CCFs, the CCF residual map against time is generated by interpolations for any given set of λ , $v \sin i$, and the other parameters for AU Mic b.

We implemented a Markov chain Monte Carlo (MCMC) analysis to estimate λ using the CCF model above. We let λ , $v \sin i$, and the transit impact parameter b float with uniform priors, and allowed the scaled semimajor axis a/R_s and mid-transit time T_c to vary with Gaussian priors (Table 1). The result of the analysis is summarized in Table 1. The reduced χ^2

Table 1
Derived Parameters for the Doppler-shadow Analysis

Parameter	Value	Prior
(derived parameters)		
λ (deg)	$-4.7^{+6.8}_{-6.4}$	$\mathcal{U}[-180, +180]$
$v \sin i$ (km s $^{-1}$)	$9.23^{+0.79}_{-0.31}$	$\mathcal{U}[5, 15]$
b	$0.18^{+0.07}_{-0.03}$	$\mathcal{U}[0, \infty]$
a/R_s	$19.34^{+0.45}_{-0.59}$	$\mathcal{N}(19.1, 1.7)$
T_c (BJD–2,458,651)	0.99275 ± 0.00061	$\mathcal{N}(0.99351, 0.00070)$
(fixed parameters)		
R_p/R_s	0.0514	
e	0	
P (days)	8.46321	

Note. The symbols \mathcal{U} and \mathcal{N} represent the uniform and Gaussian priors, respectively.

for the best-fit model is 0.87. The best-fit obliquity ($\lambda = -4.7^{+6.8}_{-6.4}$ degrees) implies a good spin–orbit alignment for the AU Mic system.

The estimated rotation velocity ($v \sin i = 9.23^{+0.79}_{-0.31}$ km s $^{-1}$) is consistent within $\approx 1.5\sigma$ with the spectroscopic value (8.7 ± 0.2 km s $^{-1}$) reported in Plavchan et al. (2020). However, those estimates are slightly larger than the expected rotation velocity at the stellar equator ($2\text{--}3\sigma$ level), inferred from the stellar radius and rotation period based on the TESS photometry ($v_{\text{eq}} = 7.81 \pm 0.31$ km s $^{-1}$). The reason for the disagreement is not known, but it suggests that (1) both spectroscopic measurements and Doppler-shadow analysis have relatively large systematic errors in $v \sin i$, (2) the stellar

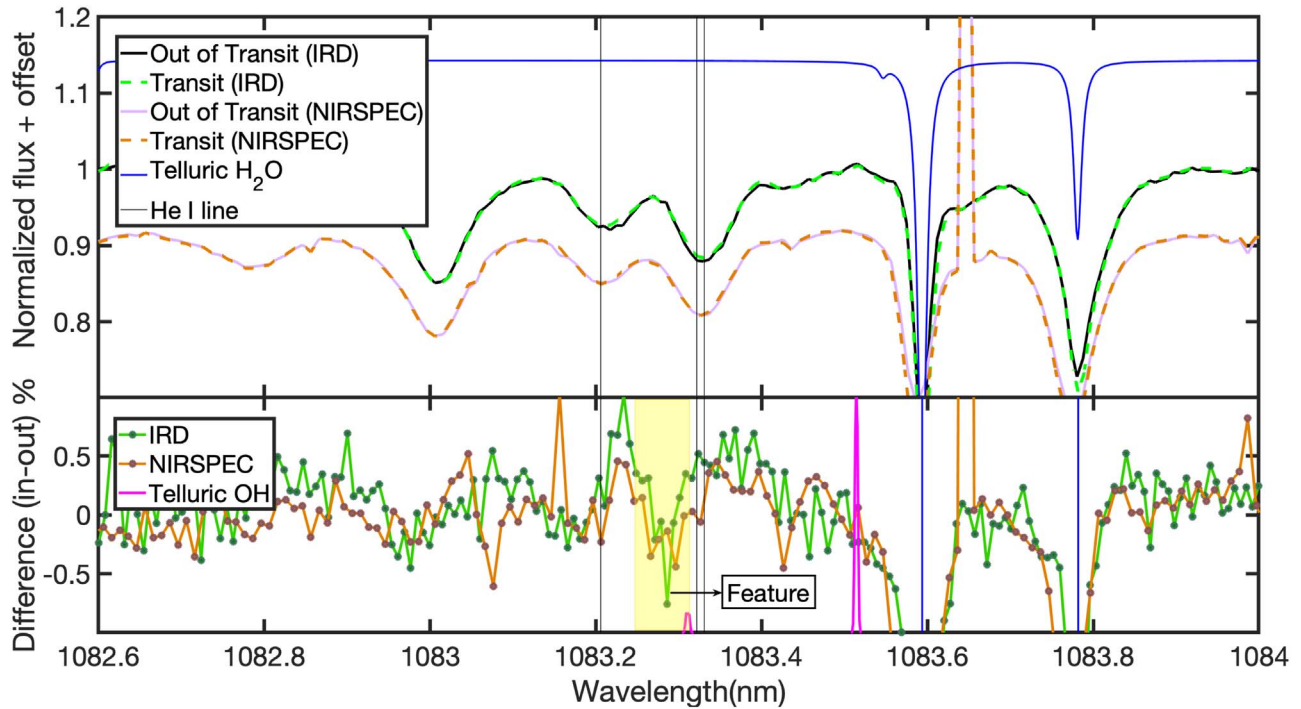


Figure 2. Top: spectra of AU Mic in the vicinity of the He I lines (vertical black lines) obtained in and out of the transit of “b” by IRD (green and black) and NIRSPEC (orange and violet). Predicted telluric H₂O (blue) lines are from Breckinridge & Hall (1973), and OH (magenta) lines are from and Noll et al. (2012) and Jones et al. (2013). Bottom: corresponding difference spectra (in–out) in percentage. The yellow-shaded region shows the ~ 0.1 nm wide feature.

radius reported in Plavchan et al. (2020) is underestimated, and/or (3) AU Mic is differentially rotating. One may be able to constrain the presence of differential rotation by continuous photometric monitoring of AU Mic.

3.3. He I Line Modeling

The unresolved $J = 1, 2$ doublet and the bluer $J = 0$ line of neutral orthohelium are both detected (Figure 2). The relative equivalent widths (EWs) suggest that the doublet is optically thick and that the absorption arises from a relatively small filling factor on the star (Andretta et al. 2017). The total EW (107 mÅ) is small for the star’s X-ray activity ($L_X/L_{\text{bol}} = -2.82$; Plavchan et al. 2009), possibly because emission partially fills in the line (Smith 2016).

We used the transit ephemeris and duration from Plavchan et al. (2020) to sum subsets of spectra inside and outside of the transit. Individual IRD spectra were adjusted to account for the varying Doppler shift of the planet ($\pm 5 \text{ km s}^{-1}$). Due to the lower resolution, this correction was unnecessary for the NIRSPEC spectra. A comparison of the summed spectra taken during transit and post-egress indicates no transit-related absorption at the wavelength of the strong doublet (Figure 2). To limit the presence of any planet-associated absorption, we assumed a Gaussian profile with thermal broadening of 1000–30,000 K for the IRD data. We adopted an rms value of 1.2% of the IRD difference spectrum for a 10 Å region in the vicinity of the line. A similar model was implemented on NIRSPEC data. Using a χ^2 analysis we limited the EW of any planet-associated signal to 4.4 and 3.7 mÅ (99% confidence) from the IRD and NIRSPEC spectra, respectively.

A ~ 0.1 nm wide feature about 0.05 nm blueward of the doublet center is apparent in both the IRD and NIRSPEC spectra (Figure 2). Since it appears in both independent data sets, it is not an artifact of the instrument or reduction routine.

Such a feature could be Doppler-shifted absorption in a gaseous tail moving relative to the star at $\approx -15 \text{ km s}^{-1}$, but it could also be a systematic, i.e., (a) telluric variation over the transit/airmass, (b) a residual from changing Doppler shift of the stellar He I line over a few hours, (c) planetary occultation of active regions of the star responsible for the He I signal, (d) changing of the stellar line shape due to active regions appearing or disappearing from the stellar limb, or (e) changes in the stellar line due to activity. We consider (a) unlikely; there are no known H₂O lines in the vicinity (Figure 2). A weak OH line coincides with the feature but should have been subtracted by the rapid beam switching during the NIRSPEC observations and other, stronger OH lines do not produce artifacts. We rule out (b) by simulating the effect, i.e., dividing the out-of-transit spectrum by a second that is Doppler shifted by the barycenter change of 440 m s^{-1} over the observation interval and finding negligible difference. We rule out (c) because we see no significant variation in the in-transit signal when binned into four intervals during the transit. We consider (d) to be unlikely because the rotation period (4.86 days) is long compared to the observation interval.

Explanation (e) remains viable because our Balmer line series measurements with SNIFS show multiple rapid rises and slower (hour-timescale) falls (Figure 3) due to variable activity including numerous small flares (Robinson et al. 2001). Flaring could produce He I emission which is blueshifted due to plasma motion (15 km s^{-1} is twice the rotational velocity of the star). The strength of the feature in IRD spectra is significantly correlated with the H α EW from SNIFS spectra (Spearman rank $\rho = 0.24$ and $p = 1.9 \times 10^{-3}$; Pearson’s $R = 0.26$ with $p = 5.0 \times 10^{-4}$), supporting this scenario (see, e.g., Guilluy et al. 2020). NIRSPEC derived values are not correlated (Spearman rank $\rho = -0.03$ and $p = 0.80$; Pearson’s $R = 0.07$ with $p = 0.53$), possibly due to lower instrument resolution and

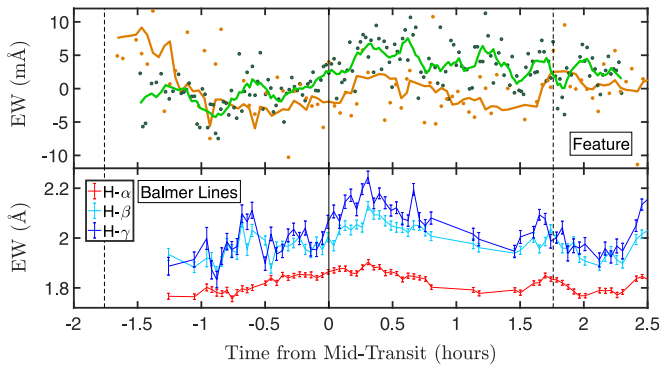


Figure 3. Top: strength of the feature between 1083.225 and 1083.325 nm versus time as measured in IRD (green) and NIRSPEC (orange) spectra. The solid lines represent seven-point, first-order Savitzky–Golay filtered versions. Bottom: equivalent width of hydrogen Balmer lines: H- α (red), H- β (aqua), and H- γ (blue) as measured in SNIFS spectra. In both panels a positive value represents increasing emission.

an early decline seen in the NIRSPEC but not the IRD data (Figure 3).

The planetary He I line was modeled with an isothermal Parker wind with a solar-like H/He ratio (10.5) as described in Gaidos et al. (2020) (see also Oklopčić & Hirata 2018). The abundance of triplet He I is governed by photoionization of ground-state He I by extreme-ultraviolet (EUV) photons and photoionization of the triplet He I by far-UV (FUV) and near-UV (NUV) photons. No complete UV spectrum of AU Mic is available, so we constructed one by combining an Extreme Ultraviolet Explorer (EUVE) spectrum (Monsignor Fossi et al. 1996) with a synthetic spectrum of the M1.5-type dwarf GJ 832 (Fontenla et al. 2016) and adjusting the EUV (90–360 Å), Ly α (1216 Å), FUV (1340–1800 Å), and NUV (1700–3000 Å) domains by an EUVE observation (France et al. 2018), Hubble Space Telescope (HST) observations (Linsky et al. 2014), and Galaxy Evolution Explorer observations analyzed by Schneider & Shkolnik (2018). The spectrum was uniformly adjusted within these wavelength ranges to match the observed fluxes. Both the sonic radius (which sets the scale of the flow) and Roche radius (beyond which it is assumed the flow is dispersed) depend on the planet mass, and through them the He I signal at a given mass loss rate is mass-dependent. The mass of “b” is not precisely determined and we considered the best-fit value to available RV data ($11.8M_{\oplus}$) and a 99% confidence upper limit ($57.3M_{\oplus}$; P. Plavchan 2020, in preparation). Figure 4 plots contours of constant EW for the two planet mass cases, showing that mass loss rates of >0.15 – $0.45 M_{\oplus} \text{ Gyr}^{-1}$ are ruled out for a wind temperature of 10,000 K, with (cooler/hotter) winds (more/less) restricted in terms of mass loss rate.

4. Discussion and Summary

At ≈ 22 Myr, the AU Mic system should not have undergone tidal spin–orbit realignment; the tidal realignment times of a Neptune-mass planet in a $P = 8.46$ day orbit is longer than a few gigayears (e.g., Winn et al. 2010; Albrecht et al. 2012), and the system should retain any primordial obliquity. Therefore, the inferred low stellar obliquity suggests that the system has not experienced an event such as planet–planet scattering (e.g., Chatterjee et al. 2008; Nagasawa & Ida 2011), and that AU Mic b likely formed in situ or migrated to its present location by torques from a primordial disk (e.g., Lin et al. 1996; Kley &

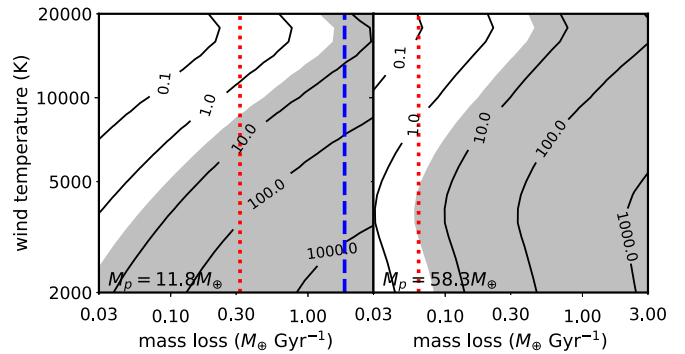


Figure 4. Contours of predicted EW in mÅ of the 1083 nm He I triplet versus mass loss rate and wind temperature for an isothermal, solar-composition model of an escaping atmosphere from AU Mic b, for the current best-fit value (left) and a 99% upper limit on planet mass based on RV data (P. Plavchan 2020, private communication). The gray region is ruled out by our transit observations. The red dotted lines are the mass loss rates for energy-limited escape, assuming 10% efficiency (Shematovich et al. 2014) and the blue dashed line is the prediction based on the hydrodynamic models of Kubyskhina et al. (2018); the estimate in the right panel is off scale to the left.

Nelson 2012). AU Mic is one of the youngest systems known to host a transiting close-in planet, making our measurements an important benchmark to compare to models of the dynamical evolution of close-in planets.

One caveat of our obliquity analysis is that the residual CCF map is affected by activity-induced variations, which we did not account for in deriving λ . AU Mic is an active, spotted star, and CCF features will evolve with spots. In addition, small flares can distort the CCF profile, and add systematic errors. Fortunately, those effects are known to be mitigated to be a factor 2–4 smaller in the infrared compared with visible due to reduced contrasts of surface spots and faculae (e.g., Crockett et al. 2012; Beichman et al. 2019). Indeed, Figure 1 does not exhibit evident spot- and flare-like features in the residual line profile. The reason for modulation seen in the H -band CCF map is not known, but we suspect it is caused by imperfect processing of telluric lines and/or the detector’s persistence, both of which are more significant in the H -band. Observations of additional transits are needed to evaluate these effects.

We detect no He I absorption during the transit of AU Mic b that could be associated with its atmosphere. A blueshifted feature is unlikely to be an artifact of our instruments, or tellurics, but appears to be the product of stellar activity. This highlights the challenge of planet transit spectroscopy for young, active stellar hosts (Cauley et al. 2018) and the imperative of obtaining simultaneous data on activity (Guilluy et al. 2020). Our limits on the atmosphere escape rate from the non-detection of He I could challenge models which explain a “Neptune desert” by X-ray and ultraviolet photoevaporative escape, primarily during the first 100 Myr when the host star is most active (Owen 2019). Loss of the $\sim 1 M_{\oplus}$ of H responsible for the large radii of Neptune-like planets in this time would require $10 M_{\oplus} \text{ Gyr}^{-1}$. AU Mic b orbits outside the “desert”; nevertheless substantial loss would be expected. We estimated escape rates using combined X-ray, EUV (90–360 Å), and Ly α irradiances (46.5 W m^{-2}) and (a) the energy-limited escape relation of Erkaev et al. (2007) with an efficiency $\eta = 10\%$ (Shematovich et al. 2014), and (b) the hydrodynamic model-based relations of Kubyskhina et al. (2018). For the best-estimate planet mass ($11.8 M_{\oplus}$) we can rule out both estimates (0.31 and $1.85 M_{\oplus} \text{ Gyr}^{-1}$) for most wind temperatures

considered (left panel of Figure 4). However, in the case of a planet mass equal to the 99% confidence upper limit ($58.3 M_{\oplus}$, right panel of Figure 4), the predicted mass loss rate would be only 0.064 and $5 \times 10^{-3} M_{\oplus} \text{ Gyr}^{-1}$ and our observations are not constraining. Refinement of the planet mass and an accounting of the effects of a non-spherical geometry, interaction with the stellar wind, and radiation pressure are needed. Unlike the case for K2-100b (Gaidos et al. 2020), our model does not predict complete photoionization of H in the wind; rather, for escape rates near the upper limit, resonant scattering by H I should produce broad ($\sim 1 \text{ \AA}$) absorption in the Ly α line during a transit and could be detected by the HST.

This work was supported by JSPS KAKENHI Grant Numbers JP19K14783, JP18H05442, JP15H02063, JP22000005, JP18H01265, and JP18H05439, JST PRESTO grant No. JPMJPR1775, and by the Astrobiology Center Program of National Institutes of Natural Sciences (NINS) (grant No. AB311017). E.G. carried out some of this research while a participant in the ‘‘ExoStar’’ program at the Kavli Institute for Theoretical Physics, which is supported in part by the National Science Foundation under Grant No. NSF PHY-1748958. E.G. thanks the UC Santa Barbara Department of Physics, especially Glenn Schiferl, for their hospitality and assistance in conducting remote observations with Keck II, and fellow observer Erik Petigura for obtaining darks and flat fields. The W. M. Keck Observatory is operated as a scientific partnership among the California Institute of Technology, the University of California and the National Aeronautics and Space Administration. The Observatory was made possible by the generous financial support of the W. M. Keck Foundation. SNIFS on the UH 2.2 m telescope is part of the Nearby Supernova Factory project, a scientific collaboration among the Centre de Recherche Astronomique de Lyon, Institut de Physique Nucléaire de Lyon, Laboratoire de Physique Nucléaire et des Hautes Energies, Lawrence Berkeley National Laboratory, Yale University, University of Bonn, Max Planck Institute for Astrophysics, Tsinghua Center for Astrophysics, and the Centre de Physique des Particules de Marseille. The data analysis was carried out, in part, on the Multi-wavelength Data Analysis System operated by the Astronomy Data Center (ADC), National Astronomical Observatory of Japan. This research made use of *Astropy*¹⁷ a community-developed core *Python* package for Astronomy (Astropy Collaboration et al. 2018), and provided by the High Energy Astrophysics Science Archive Research Center (HEASARC), which is a service of the Astrophysics Science Division at NASA/GSFC.

Facilities: Subaru(IRD), Keck II(NIRSPEC).

Software: IRAF (Tody 1993).

Appendix Analysis of the Effective RVs

RVs for AU Mic, derived in Section 3.1, are plotted in Figure 5. The typical internal RV error during the night was $8\text{--}10 \text{ m s}^{-1}$. In order to constrain the projected stellar obliquity λ , we fitted the observed RVs using the analytic RM model by Hirano et al. (2011). Since the obliquity measurement by fitting the effective RVs sensitively depends on the RV baseline, we allowed the RV semi-amplitude K by the Keplerian planetary orbit to float freely, assuming a circular orbit. Although

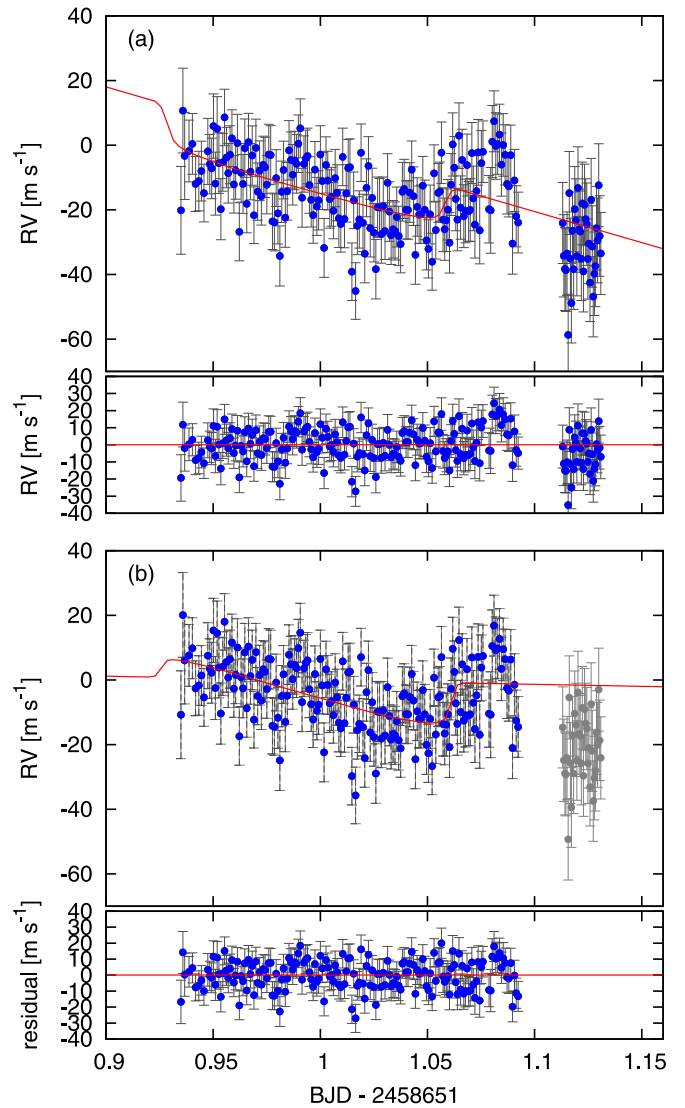


Figure 5. Results of the RV analysis and modeling of the effective RVs for the RM effect. Panel (a) presents the result of the RM fit using all the RV data during the transit night, while panel (b) shows the fitting result for the RV data set before observing the telluric standard star. In both fits, a Gaussian prior is imposed on $v \sin i$.

Plavchan et al. (2020) reported a constraint on AU Mic b’s mass from the RV monitoring, we do not use any prior information on the RV variation due to the lack of knowledge on the instantaneous RV variations by stellar activity, especially for the wavelength range covered by IRD.

We first attempted to fit all the observed RVs during the night without a prior on $v \sin i$. Due to the lack of the transit ingress and RV baseline, however, the fit did not converge, exhibiting a strong correlation among K , $v \sin i$, and λ . We thus decided to impose a prior on $v \sin i$ based on spectroscopy. Following Hirano et al. (2020a), we analyzed the mean out-of-transit CCF of the IRD spectra for AU Mic, and derived $v \sin i$ by comparing the observed CCF with a number of theoretically simulated CCFs for different $v \sin i$. The fitting result suggests $v \sin i = 8.38^{+0.19}_{-0.17} \text{ km s}^{-1}$, which is compatible with the value reported in the discovery paper ($v \sin i = 8.7 \pm 0.2 \text{ km s}^{-1}$). To take into account the systematic error in the derived $v \sin i$, especially arising from the uncertainty in the stellar macro-turbulent velocity, we enlarged the error bar for $v \sin i$ and















¹⁷ <http://www.astropy.org>

employed the Gaussian prior of $v \sin i = 8.4 \pm 0.4 \text{ km s}^{-1}$ in the RM fit. In fitting the observed RVs by the MCMC analysis, we also imposed Gaussian priors on the mid-transit time ($T_c = 2458651.99351 \pm 0.00070$), the scaled semimajor axis ($a/R_s = 19.1 \pm 1.7$), and the transit impact parameters ($b = 0.16 \pm 0.14$) based on the values in Plavchan et al. (2020). The optimized parameters in the MCMC analysis are K , $v \sin i$, λ , T_c , a/R_s , b , and RV offset γ for the IRD data set.

The red solid line in panel (a) of Figure 5 draws the best-fit model for the observed RVs. The model yielded $\lambda = 91 \pm 5$ deg, suggesting a significant spin-orbit misalignment of the system. However, the model also implied $K = 260^{+33}_{-36} \text{ m s}^{-1}$, which is inconsistent with what Plavchan et al. (2020) found. This unusually large K made us wonder whether our analysis of the observed RVs could be affected by the systematic effects associated with the lack of baseline data. Specifically, the RV data points beyond $\text{BJD}-2,458,651 = 1.1$ are mostly responsible for the large K , but those IRD spectra were taken with very high airmass at the very end of the night during twilight. We thus performed the same analysis above only using RV data before $\text{BJD}-2,458,651 = 1.1$, and derived the obliquity λ along with the other parameters. The MCMC fit for this case resulted in $K = 17^{+75}_{-73} \text{ m s}^{-1}$ and $\lambda = 69^{+7}_{-8}$ degrees. Its best-fit model is shown by the red solid line in panel (b) of Figure 5.

Lastly, we repeated the MCMC analysis for the limited set of RV data ($\text{BJD}-2,458,651 < 1.1$) without a prior on $v \sin i$. Although the posterior distribution still shows a degeneracy between $v \sin i$ and λ , a relatively small value was favored for K . We obtained $\lambda = -45^{+114}_{-81}$ deg and $v \sin i = 7.5^{+17.4}_{-2.8} \text{ km s}^{-1}$ from the MCMC fit. The results of all these analyses suggest that the stellar obliquity estimated from our RV data sensitively depends on both $v \sin i$ and the overall RV baseline during the night, and it is not straightforward to gain a reliable (accurate) estimate for λ , mostly owing to the lack of baseline RV data. Therefore, we decided not to use the RV data and resorted to an alternative approach (Doppler-shadow analysis) for the measurement of λ .

ORCID iDs

Teruyuki Hirano  <https://orcid.org/0000-0003-3618-7535>
 Eric Gaidos  <https://orcid.org/0000-0002-5258-6846>
 Heather Flewelling  <https://orcid.org/0000-0002-1050-4056>
 Andrew W. Mann  <https://orcid.org/0000-0003-3654-1602>
 Norio Narita  <https://orcid.org/0000-0001-8511-2981>
 Peter Plavchan  <https://orcid.org/0000-0002-8864-1667>
 Motohide Tamura  <https://orcid.org/0000-0002-6510-0681>
 Hiroki Harakawa  <https://orcid.org/0000-0002-6197-5544>
 Klaus Hodapp  <https://orcid.org/0000-0003-0786-2140>
 Masato Ishizuka  <https://orcid.org/0000-0003-1906-4525>
 Mihoko Konishi  <https://orcid.org/0000-0003-0114-0542>
 Tomoyuki Kudo  <https://orcid.org/0000-0002-9294-1793>
 Masayuki Kuzuhara  <https://orcid.org/0000-0002-4677-9182>
 Jun Nishikawa  <https://orcid.org/0000-0001-9326-8134>

References

Albrecht, S., Winn, J. N., Johnson, J. A., et al. 2012, *ApJ*, 757, 18

- Andretta, V., Giampapa, M. S., Covino, E., Reiners, A., & Beeck, B. 2017, *ApJ*, 839, 97
- Astropy Collaboration, Price-Whelan, A. M., Sipőcz, B. M., et al. 2018, *AJ*, 156, 123
- Beichman, C., Hirano, T., David, T. J., et al. 2019, *RNAAS*, 3, 89
- Breckinridge, J. B., & Hall, D. N. B. 1973, *SoPh*, 28, 15
- Cauley, P. W., Kuckein, C., Redfield, S., et al. 2018, *AJ*, 156, 189
- Chatterjee, S., Ford, E. B., Matsumura, S., & Rasio, F. A. 2008, *ApJ*, 686, 580
- Collier Cameron, A., Guenther, E., Smalley, B., et al. 2010, *MNRAS*, 407, 507
- Crockett, C. J., Mahmud, N. I., Prato, L., et al. 2012, *ApJ*, 761, 164
- David, T. J., Hillenbrand, L. A., Petigura, E. A., et al. 2016, *Natur*, 534, 658
- David, T. J., Petigura, E. A., Luger, R., et al. 2019, *ApJL*, 885, L12
- Erkaev, N. V., Kulikov, Y. N., Lammer, H., et al. 2007, *A&A*, 472, 329
- Fabrycky, D., & Tremaine, S. 2007, *ApJ*, 669, 1298
- Fontenla, J. M., Linsky, J. L., Witbrod, J., et al. 2016, *ApJ*, 830, 154
- France, K., Arulanantham, N., Fossati, L., et al. 2018, *ApJS*, 239, 16
- Fulton, B. J., Petigura, E. A., Howard, A. W., et al. 2010, *AJ*, 154, 109
- Gaidos, E., Hirano, T., Mann, A. W., et al. 2020, *MNRAS*, 495, 650
- Ginzburg, S., Schlichting, H. E., & Sari, R. 2018, *MNRAS*, 476, 759
- Grady, C. A., Wisniewski, J. P., Schneider, G., et al. 2020, *ApJL*, 889, L21
- Guillou, G., Andretta, V., Borsari, F., et al. 2020, *A&A*, 639, A49
- Hirano, T., Gaidos, E., Winn, J. N., et al. 2020a, *ApJL*, 890, L27
- Hirano, T., Kuzuhara, M., Kotani, T., et al. 2020b, arXiv:2007.11013
- Hirano, T., Suto, Y., Taruya, A., et al. 2010, *ApJ*, 709, 458
- Hirano, T., Suto, Y., Winn, J. N., et al. 2011, *ApJ*, 742, 69
- Johnson, M. C., Cochran, W. D., Addison, B. C., Tinney, C. G., & Wright, D. J. 2017, *AJ*, 154, 137
- Jones, A., Noll, S., Kausch, W., Szyszka, C., & Kimeswenger, S. 2013, *A&A*, 560, A91
- Kley, W., & Nelson, R. P. 2012, *ARA&A*, 50, 211
- Kotani, T., Tamura, M., Nishikawa, J., et al. 2018, *Proc. SPIE*, 10702, 1070211
- Kubyskhina, D., Fossati, L., Erkaev, N. V., et al. 2018, *ApJL*, 866, L18
- Kuzuhara, M., Hirano, T., Kotani, T., et al. 2018, *Proc. SPIE*, 10702, 1070260
- Lantz, B., Aldering, G., Antilogus, P., et al. 2004, *Proc. SPIE*, 5249, 146
- Lin, D. N. C., Bodenheimer, P., & Richardson, D. C. 1996, *Natur*, 380, 606
- Linsky, J. L., Fontenla, J., & France, K. 2014, *ApJ*, 780, 61
- Lundkvist, M. S., Kjeldsen, H., Albrecht, S., et al. 2016, *NatCo*, 7, 11201
- Mamajek, E. E., & Bell, C. P. M. 2014, *MNRAS*, 445, 2169
- Mann, A. W., Gaidos, E., Mace, G. N., et al. 2016a, *ApJ*, 818, 46
- Mann, A. W., Johnson, M. C., Vanderburg, A., et al. 2020, arXiv:2005.00047
- Mann, A. W., Newton, E. R., Rizzuto, A. C., et al. 2016b, *AJ*, 152, 61
- Mann, A. W., Vanderburg, A., Rizzuto, A. C., et al. 2018, *AJ*, 155, 4
- McLean, I. S., Becklin, E. E., Bendiksen, O., et al. 1998, *Proc. SPIE*, 3354, 566
- Monsignorini Fossi, B. C., Landini, M., Del Zanna, G., & Bowyer, S. 1996, *ApJ*, 466, 427
- Nagasawa, M., & Ida, S. 2011, *ApJ*, 742, 72
- Newton, E. R., Mann, A. W., Tofflemire, B. M., et al. 2019, *ApJL*, 880, L17
- Noll, S., Kausch, W., Barden, M., et al. 2012, *A&A*, 543, A92
- Oklopčić, A., & Hirata, C. M. 2018, *ApJL*, 855, L11
- Owen, J. E. 2019, *AREPS*, 47, 67
- Plavchan, P., Barclay, T., Gagné, J., et al. 2020, *Natur*, 582, 497
- Plavchan, P., Werner, M. W., Chen, C. H., et al. 2009, *ApJ*, 698, 1068
- Quinn, S. N., White, R. J., Latham, D. W., et al. 2012, *ApJL*, 756, L33
- Robinson, R. D., Linsky, J. L., Woodgate, B. E., & Timothy, J. G. 2001, *ApJ*, 554, 368
- Sato, B., Izumiura, H., Toyota, E., et al. 2007, *ApJ*, 661, 527
- Schneider, A. C., & Shkolnik, E. L. 2018, *AJ*, 155, 122
- Shematovich, V. I., Ionov, D. E., & Lammer, H. 2014, *A&A*, 571, A94
- Smith, G. H. 2016, *PASA*, 33, e057
- Spalding, C., & Batygin, K. 2016, *ApJ*, 830, 5
- Tamura, M., Suto, H., Nishikawa, J., et al. 2012, *Proc. SPIE*, 8446, 84461T
- Tody, D. 1993, J. in ASP Conf. Ser. 52, *Astronomical Data Analysis Software and Systems II*, ed. R. J. Hanisch, R. J. V. Brissenden, & J. Barnes (San Francisco, CA: ASP), 173
- Vazan, A., Ormel, C. W., & Dominik, C. 2018, *A&A*, 610, L1
- Winn, J. N., Fabrycky, D., Albrecht, S., & Johnson, J. A. 2010, *ApJL*, 718, L145
- Winn, J. N., Noyes, R. W., Holman, M. J., et al. 2005, *ApJ*, 631, 1215